



HAL
open science

Multielectron coincidence spectroscopy of the $\text{Ar } 2 + (2p - 2)$ double-core-hole decay

Maximilian Mailhiot, Kari Jänkälä, Marko Huttula, Minna Patanen, Klemen Bučar, Matjaž Žitnik, Denis Cubaynes, Fabian Holzmeier, Raimund Feifel, Denis Céolin, et al.

► **To cite this version:**

Maximilian Mailhiot, Kari Jänkälä, Marko Huttula, Minna Patanen, Klemen Bučar, et al.. Multielectron coincidence spectroscopy of the $\text{Ar } 2 + (2p - 2)$ double-core-hole decay. *Physical Review A*, 2023, 107 (6), pp.063108. 10.1103/PhysRevA.107.063108 . hal-04284339

HAL Id: hal-04284339

<https://hal.science/hal-04284339v1>

Submitted on 14 Nov 2023

HAL is a multi-disciplinary open access archive for the deposit and dissemination of scientific research documents, whether they are published or not. The documents may come from teaching and research institutions in France or abroad, or from public or private research centers.

L'archive ouverte pluridisciplinaire **HAL**, est destinée au dépôt et à la diffusion de documents scientifiques de niveau recherche, publiés ou non, émanant des établissements d'enseignement et de recherche français ou étrangers, des laboratoires publics ou privés.

Multielectron coincidence spectroscopy of the Ar^{2+} ($2p^{-2}$) double-core-hole decay

Maximilian Mailhiot ^{1,7,*}, Kari Jänkälä ¹, Marko Huttula ¹, Minna Patanen ¹, Klemen Bučar ², Matjaž Žitnik ², Denis Cubaynes³, Fabian Holzmeier^{4,†}, Raimund Feifel ⁵, Denis Céolin ⁶, Lidija Andric⁷, Renaud Guillemin ⁷, Iyas Ismail ⁷, Jerome Palaudoux ⁷, Francis Penent ⁷ and Pascal Lablanquie ⁷

¹Nano and Molecular Systems Research Unit (NANOMO), Faculty of Science, University of Oulu, P.O. Box 3000, FIN-90014 Oulu, Finland

²J. Stefan Institute, Jamova 39, SI-1000 Ljubljana, Slovenia

³Institut des Sciences Moléculaires d'Orsay, Centre National de la Recherche Scientifique, Bâtiment 520 Université Paris-Sud and Paris-Saclay, F-91405 Orsay Cedex, France

⁴Dipartimento di Fisica, Politecnico di Milano, I-20133 Milano, Italy

⁵University of Gothenburg, Department of Physics, SE-41258 Gothenburg, Sweden

⁶Synchrotron SOLEIL, L'Orme des Merisiers, Départementale 128, F-91190 Saint-Aubin, France

⁷Laboratoire de Chimie Physique Matière et Rayonnement, Sorbonne Université and Centre National de la Recherche Scientifique, F-75005 Paris, France



(Received 28 March 2023; accepted 2 June 2023; published 23 June 2023)

The dominant decay pathways of argon $2p^{-2}$ double-core-hole states have been investigated using synchrotron radiation and a magnetic-bottle-type spectrometer coupled with an ion time-of-flight spectrometer. This experiment allows for efficient multi-electron-ion coincidence measurements, and thus for following the Auger cascade step by step in detail. Dominant decay pathways leading to Ar^{4+} final states via Ar^{3+} intermediate states have been assigned with the help of theoretical *ab initio* calculations. The weak correlated decay of the two core holes by emission of a single Auger electron, leading to Ar^{3+} final states, has been observed at 458.5-eV kinetic energy. Compared to the total decay of the $2p^{-2}$ double core vacancies, this two-electron–one-electron process was measured to have a branching ratio of $1.9 \times 10^{-3} \pm 1.0 \times 10^{-3}$. Furthermore, the remaining decay paths of the Ar^{1+} ($1s^{-1}$) core hole to higher charge states and their respective contributions to the total yield have been analyzed and show very good agreement with theoretical results.

DOI: [10.1103/PhysRevA.107.063108](https://doi.org/10.1103/PhysRevA.107.063108)

I. INTRODUCTION

Double core holes (DCHs) of the K shell were first observed by Charpak *et al.* [1] in their study of electron capture in ^{55}Fe . Later on, the radiative decay of DCHs created by synchrotron radiation was investigated by Hoszowska *et al.* [2].

In 1986, Cederbaum *et al.* [3] predicted enhanced chemical shifts for double-core-hole states, which was confirmed much later by synchrotron light experiments on small molecules like CO, N_2 [4,5], NO and N_2O [6], C_2H_2 [7], and benzene [8–10]. Comprehensive overviews of the results obtained by these experiments have been published by Penent *et al.* [11] and Lablanquie *et al.* [12].

Recently, the focus has broadened to include the study of hypersatellites ($K^{-2}V$), which also involves probing of dipole-forbidden core-hole transitions. Notably, studies utilizing a magnetic bottle spectrometer have been done on C_2H_{2n} [13], H_2O [14], N_2 [15], and CO_2 [16], revealing that the conjugate channel exhibits comparable intensity to the direct shake-up channel. Electron spectroscopy studies on hollow lithium have been done by Journal *et al.* [17] and Diehl *et al.* [18,19] (following previous work by Ref. [20]),

demonstrating the possibility to observe these states without relying on coincidence measurement techniques. Goldsztejn *et al.* [21,22] have analyzed Ne DCHs, likewise without applying coincidence techniques. Additionally, Püttner *et al.* [23] and Koulentianos *et al.* [24] studied $K^{-2}V$ states in Ar and HCl, respectively. Recently, the cross sections of the charge states resulting after K shell single and double ionization of C^- [25] and O^- [26] have been studied, as well as the charge states resulting from one-photon single and double ionization of the L shell of Ar^+ [27].

Studies of DCHs are still a challenging task from the experimental and theoretical point of view. Experimentally, a low cross section for creation of the double vacancies with absorption of a single photon and the subsequent isolation of their signal pose significant challenges. It should be noted that double ionization by absorption of a single photon [4,5] is about 10^{-3} times less likely than single ionization [5]. On the other hand, x-ray free electron lasers (XFELs) provide the necessary intensity for efficient multiphoton ionization, leaving behind the DCH states. Studies using XFELs have been done, e.g., on CO [28], Ne [29], and several small molecules [29,30]. While it is possible to study correlations between the emitted particles by covariant mapping [31] using XFELs, the well-established coincidence techniques used at synchrotron facilities are highly beneficial for isolating the DCH signatures from the prevailing direct single Auger decay and other processes with spectral overlap. However, to

*Corresponding author: maximilian.mailhiot@oulu.fi

†Present address: Imec, Kapeldreef 75, BE-3001 Leuven, Belgium.

reliably identify DCH states, threefold or higher coincidences are needed, making an instrument like the magnetic-bottle-type spectrometer, which is capable of collecting electrons from almost the whole 4π steradian, almost mandatory.

In the present paper, we show a way of studying double core holes at synchrotrons with a magnetic bottle, enabling us to analyze the decay path in full detail. The double core holes in the L shell of argon atoms are efficiently created by Auger decay of single K shell holes, thereby circumventing the low cross sections of direct double ionization processes. Although this technique is not applicable for elements of the second row or for the study of K^{-2} states, it has the advantage in studies of less tightly bound DCHs in heavier elements.

Concerning decay of the argon $1s^{-1}$ states, studies of the main KLL - and KLM -Auger transitions have been done by Asplund *et al.* [32] in 1977, while Omar and Hahn [33] have predicted the relative final ion yield in 1992. More recently, Guillemin *et al.* analyzed the decay pathways following $1s$ ionization in detail, both experimentally [34,35] and in comparison to theory [36]. Wang *et al.* [37] gave a further theoretical prediction of the final ion yield.

A theoretical prediction on the decay of argon L shell DCHs created by two subsequent photoionization events exists [38], but it was suggested it would only be possible to be tested in hopefully available coincidence experiments with XFEL light pulses in the future. Our experiment allows for a direct test with relatively weak synchrotron light.

In the present paper, argon has been chosen as a showcase, but our method is generally applicable for all atoms and molecules where DCHs are formed by decays of deeper inner shells [39]. Of specific interest in the present context would be the HCl and H₂S molecules, since they are isoelectronic to argon, and similar spectroscopic signatures are thus expected.

II. EXPERIMENTAL APPARATUS AND PROCEDURE

The experiment was performed at the GALAXIES [40] hard x-ray beamline at the SOLEIL synchrotron facility in France. A detailed description of the experimental gas-phase end station that was used can be obtained elsewhere [41].

The spectra were recorded with a magnetic bottle time-of-flight spectrometer based on the kind developed by Eland *et al.* [42]. The specifications of the present instrument have been described elsewhere [43], and the details on its modification for ion detection, and a schematic of the setup, can be found in Fig. 2 of a recent publication by Ismail *et al.* [44]. However, for the sake of simplicity, our choice in the present experiment was to use a constant extraction potential of 3 V instead of a pulsed ion extraction of 200 V that could generate parasitic signals on the rising edge of the extraction pulse (due to radiative, inductive, or capacitive coupling). Further, the plate in front of the magnet was placed at a distance of about 3 mm from the gas-introducing needle, instead of 2 mm in Ref. [44]. The instrument uses a permanent magnet (field strength ≈ 0.5 T) that acts as a magnetic mirror and confines the electrons into an ≈ 2 -m-long drift tube which is surrounded by a homogeneous solenoid for guiding the electrons towards the detector [microchannel plate (MCP) stack]. The field strength in the drift tube is about 1 mT. In the opposite direction from the target, a 4-mm hole in the

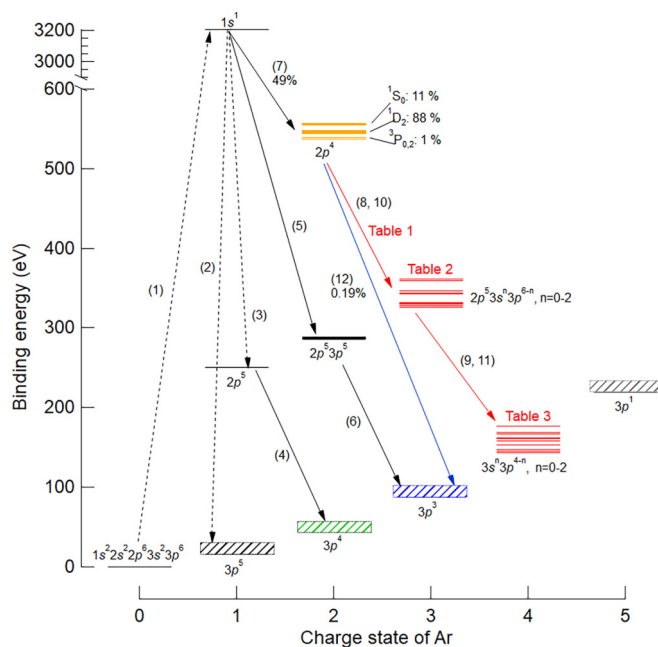


FIG. 1. The (simplified) energy diagram of the discussed states. After $1s$ ionization (ionization energy of 3206.26 eV given by Ref. [46]), KLL -Auger decay to $2p^{-2}$ DCH levels takes place. The intensities of the levels of the $2p^{-2}$ DCH are given by Ref. [62]. Only two (1S_0 and 1D_2) of these levels were sufficiently intense to be measured. The decay from $2p^{-2}$ to Ar⁵⁺ final states (threshold 219 eV [65]) could not be observed although it is energetically possible. The numbers in brackets refer to the equations in the text. Transitions including photons are represented by dashed lines.

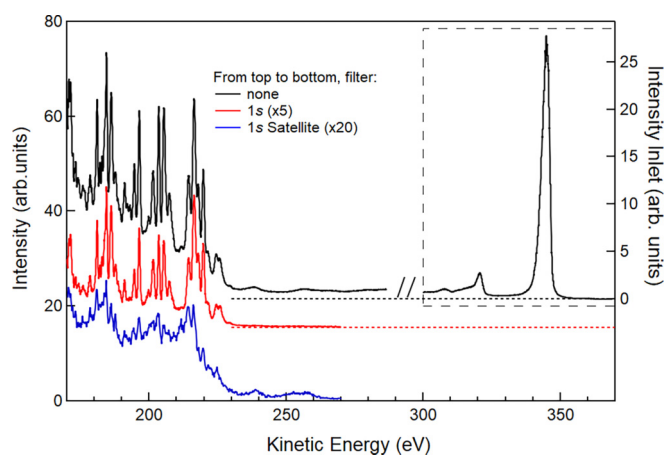


FIG. 2. The experimental unfiltered electron spectrum (black line) in the region of interest (i.e., the region that contains the main Auger lines associated with $2p^{-2}$ decay) is compared to the measured spectrum filtered by the $1s$ photoelectron signal at 344 eV (red line) or by the corresponding satellite signal at 320-eV (blue line) kinetic energy. For better visibility, an offset for the full electron spectrum and the spectrum filtered with respect to the $1s$ photoelectron has been introduced. The zero intensity levels are indicated by dashed lines. An inset surrounded by a dashed box indicates the $1s$ electron and its satellite with unchanged kinetic-energy scale and the intensity given by the left axis.

permanent magnet allows the ions to fly into a short (≈ 15 cm) electrostatic time-of-flight tube. The positive ions are repelled by a mesh at a potential of +3 V at 10 mm from the hole. Because the photon beam crosses the effusive gas beam at a position ≈ 3 mm from the magnet, the Ar^{4+} ions acquire a kinetic energy of $\approx q \times 1$ eV when they enter the hole. They are then accelerated to 1 keV by a set of electrodes polarized with a resistive voltage divider in a 12-cm flight tube, and finally to ≈ 2 keV at the front of the MCP to allow for efficient detection of the ions. The MCP back is set to a potential of $\approx +200$ V via a 1-to-10 resistive voltage divider and the signal is collected on a grounded metallic anode by capacitive decoupling. The constant extraction field of 3 V/cm generates a potential change of 100 mV across the interaction region defined by the photon beam size of about 300 μm . This reduces the electron energy resolution by 100 meV.

The flight times of both ions and electrons are measured by a time-to-digital converter (TDC), which compares the arrival times to the ring clock of the synchrotron. Because the single pulse period at SOLEIL is 1184 ns, the ring clock is not directly suitable for measuring longer flight times without overlap from the next pulses. Instead, a chopper was used, which extended the time interval between two pulses to about 10 μs . The ring clock was validated by a channeltron detector, which registered light pulses that passed the chopper (see Ref. [45] for more details).

The spectra were measured at 3550-eV photon energy, well above the $1s$ ionization threshold of argon at (3206.26 ± 0.3) eV [46]. The electrons were decelerated by a voltage of +165 V applied to the 2-m-long electron drift tube. The deceleration occurs in a 3-mm distance between two high transparency ($\approx 95\%$) gold grids, the first one being grounded and the second one at the potential of the drift tube. This avoids any eventual lensing depending on electron energy. This deceleration method has been previously reported about in Ref. [9].

The well-studied *LMM* decay of $\text{Ar}^{1+}(2p^{-1})$ states to $\text{Ar}^{2+}(3p^4)$ states [47,48] was used for calibration, in addition to the primary $\text{Ar}^{1+}(1s^{-1})$ to $\text{Ar}^{2+}(2p^{-2} \ ^1D_2)$ *KLL* peak at 2660.5 eV [32].

By comparing the total count rates with the count rates in coincidence with the final ionic charge states or other electrons emitted with specific kinetic energies, the detection efficiencies were estimated. It turned out that ions of all charges were detected with an efficiency of about 10%, except for doubly charged ions, which had about 12% detection efficiency. Electrons were detected with an efficiency of about 20% at a kinetic energy of 20 eV, 12% at 200 eV, and 1.3% at 3000 eV, which is less than previously reached with this setup and was due to an unintendedly high MCP signal threshold. The resolution in the main region of studied electron kinetic energies (180–240 eV) was approximately 600 meV.

III. COMPUTATIONAL DETAILS

The calculations were carried out using Flexible Atomic Code (FAC) [49]. The program was run in relativistic Dirac-Fock-Slater configuration-interaction mode. In this method, the atomic states are modeled as linear combinations of configuration state functions, which in turn are antisymmetrized

jj-coupled linear combinations of N -electron Slater determinants. The radial parts of the one-electron wave functions in the system were optimized in the average energy-level scheme via the self-consistent field Dirac-Fock method and the weight coefficients of the configuration state functions were obtained by diagonalizing the relativistic Hamiltonian operator. For details on the method, see Ref. [50].

The states for each Auger decay step leading from Ar^{2+} to Ar^{4+} were constructed by including all levels from all possible electronic configurations of orbitals occupied in the ground state of Ar which are energetically allowed in the single configuration approximation. In addition, configuration interaction was added by allowing single and double excitations to the $3d$ orbital from $3s$ and $3p$ orbitals. For the sake of simplicity, the Ar^{1+} case was modeled in the single configuration approximation. In the cases of Ar^{2+} and Ar^{3+} , the calculations were divided into two groups, one of which included at least one L orbital hole and one that had all L orbitals closed. This was done because the two groups of levels are far apart in energy, leading to negligible configuration interaction and at the same time causing problems in describing the states with average level optimization. The total size of configuration space in the case of Ar^{1+} was 1, in Ar^{2+} 793, in Ar^{3+} 1269, and in Ar^{4+} 225.

The matrix elements of the Auger decay were calculated using the standard Coulomb operator formulation, described for instance in Ref. [51] and references therein. In the case of calculating a large number of Auger transitions, solving the continuum wave function individually for each decay can be a highly time-consuming task. In using FAC, this problem is solved by approximating the continuum wave close to the nucleus by a highly excited bound orbital [49]. This provides a considerable speed-up and was seen to provide sufficient accuracy in the present case.

IV. RESULTS AND DISCUSSION

A. Coincidence results and possible decay paths after $1s$ ionization

In order to isolate the decay processes of the $\text{Ar}^{2+}(2p^{-2})$ DCHs, careful coincidence selection is necessary. To guide the reader through this selection and the plethora of possible decay pathways after $1s$ ionization, Fig. 1 provides an overview, including the corresponding equation numbers from the text. While we are mainly interested in the decay of the DCH, we first give a summary of all other possible pathways for $1s^{-1}$ decay, to understand their spectroscopic signature and thus be able to eliminate them from the final data.

First, however, we have to ensure that $1s$ ionization does indeed occur. Besides the $1s$ shell, the selected photon energy is high enough to cause transitions involving the satellite states accompanying the $1s$ main line, and also less strongly bound $2s$ and $2p$ shells can be ionized, despite much smaller photoionization cross sections at 3550 eV. Figure 2 shows the raw experimental spectrum in the well-known *LMM*-Auger electron kinetic-energy range 180–270 eV, and the results in the same region in coincidence with the $1s$ photoelectron or the accompanying $1s^{-1} 3p^{-1} 4p$ satellite structure at 320-eV kinetic energy (assignment according to Ref. [52]). The result

for the main Auger lines until about 230 eV is remarkably similar between the latter two, except for the lower intensity in case of the signal in coincidence with the satellite. It follows that the $1s$ satellite decay is largely a spectator decay of the core, leaving the Auger electron's energy practically unchanged. Importantly, the Auger decay of the $1s$ to $4p$ resonance [36] partly leads to population of the same configurations as the satellite spectator Auger decay does [e.g., the Ar^{2+} ($2p^5 3p^4 4p^1$) configuration reached after *KLM* satellite Auger decay of the satellite and *KLL*-Auger decay followed by *LMM*-Auger decay of the $1s$ to $4p$ resonance]. Because similar features are observed in both cases, it can indeed be confirmed that the satellite decay can largely be understood in terms of spectator Auger decay. However, this picture breaks down for higher Auger energies, where the spectrum corresponding to the satellite decay exhibits two broad peaks centered at around 240 and 255 eV, which are not present in the decay in coincidence with the $1s$ photoelectron. These two peaks are in coincidence with Ar^{4+} ions and potentially correspond to participator Auger decay to Ar^{3+} ($2p^5 3s^1 3p^5$) and ($2p^5 3p^4$) intermediate configurations, which then further decay, yielding Ar^{4+} ions. Notably, Lablanquie *et al.* [53] measured a similar structure at 229 eV in case of argon $2p^{-1}$ satellite decay that remains unassigned.

In order to eliminate these high-energy contributions, we filter all following spectra with respect to the measured kinetic energy of the photoelectron (≈ 344 eV). Accordingly, Fig. 2 shows in red only decay after $1s$ ionization.

A knock-down transition of the satellites leading to $2p^{-2}$ DCH states is possible [54], but was measured to amount to only 0.5% of the overall satellite decay [54].

Second, we filter the whole set of decay pathways after $1s$ ionization by final ionic charge [Fig. 3(b)] and compare to calculations [Fig. 3(a)]. The electrons are measured in coincidence with the ion charge state at the end of the decay path, even if those electrons were emitted during intermediate decay steps. This is due to the lifetime of Ar^{1+} ($1s^{-1}$) being approximately 1 fs [35,55], that of Ar^{2+} ($2p^{-2}$) being 2.8 fs [35,55], and the longest lifetimes of the intermediate states of the Ar^{3+} to Ar^{4+} transitions being on the order of picoseconds [56], all of which are much shorter than the lifetime of the experimental time of flight (on the order of microseconds). The calculations are likewise arranged according to the final ionic charge, for easier comparison. The results can be compared to Guillemin *et al.* [36], who also studied the decay of argon after $1s$ ionization. However, using a single hemispherical Scienta electron analyzer they could not implement electron coincidence filtering techniques. Hence, their spectra are possibly affected by the signal from decay of less strongly bound shells, as described above. Further, Guillemin *et al.* could not filter the spectra with respect to the final ionic charge. They had to rely on comparing their experimental spectrum to the sum of the calculated electron yield for each decay path. The use of a coincidence setup, however, allows us to directly compare each decay pathway to theory, but this comes at the cost of reduced spectral resolution, as Guillemin *et al.* reported a spectrometer resolution of 180 meV, compared to 600 meV in our case. Since comparison of our experimental data to their original theory revealed significant differences, especially for the Auger electrons with kinetic energies in the 190–200-eV

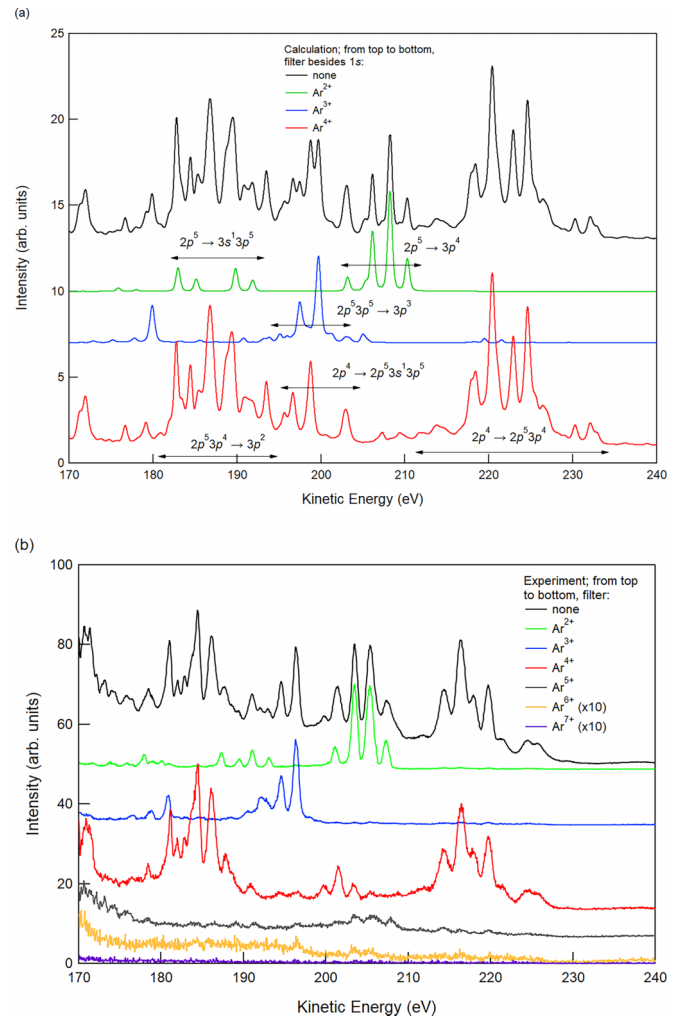


FIG. 3. The calculated theoretical (a) and experimental spectra (b) in the kinetic-energy range from 170 to 240 eV, filtered by coincidence detection of the final ion charge. The calculations are improved versions of those previously published in Ref. [36].

range that are related to decay pathways leading to Ar^{3+} and Ar^{4+} , we decided to carry out another set of calculations. Figure 3 shows our improved calculations together with the experimental results. The agreement between experiment and theory is generally very good (see details below).

Figure 3 displays the Auger spectra associated with 2+ to 7+ final ion charges. In the following, the pathways to reach these charge states are presented. In principle, the electronic ground state of singly charged argon can be reached via radiative decay, namely the $K\beta$ decay [35]:

$$\gamma(3550 \text{ eV}) + \text{Ar} \rightarrow \text{Ar}^{1+}(1s^1) + e_{\text{Photo}}^- (\approx 344 \text{ eV}), \quad (1)$$

$$\text{Ar}^{1+}(1s^1) \rightarrow \text{Ar}^{1+}(3p^5) + \gamma [\approx 3190 \text{ eV} (\text{see Ref. [57]})]. \quad (2)$$

However, since we cannot measure the emitted photon with the present setup, pathway (2) is absent from the experiment and calculations. For clarity, it is shown in Fig. 1 with a dashed line. The probability of this decay has been reported to be 0.9% of the overall $1s$ hole decay [36].

In general, radiative decay of the argon $1s$ hole has been estimated to constitute in total between 10.6% [34,36] and 11.2% [58] of the overall decay. The majority (78.3%) [36] of radiative decay is leading to Ar^{2+} ions via $K\alpha$ decay (also shown by a dashed line in Fig. 1):

$$\gamma(3550 \text{ eV}) + \text{Ar} \rightarrow \text{Ar}^{1+}(1s^1) + e_{\text{Photo}}^- (\approx 344 \text{ eV}), \quad (3)$$

$$\text{Ar}^{1+}(1s^1) \rightarrow \text{Ar}^{1+}(2p^5) + \gamma[\approx 2958 \text{ eV}(\text{see Ref. [57]})], \quad (4)$$

$$\begin{aligned} \text{Ar}^{1+}(2p^5) \rightarrow \text{Ar}^{2+}(3p^4), (3s^1 3p^5) \\ + e_{\text{Auger}}^- (\approx 205 \text{ eV})[e_{\text{Auger}}^- (190 \text{ eV})], \end{aligned} \quad (5)$$

with zero or one $3s$ holes. Decay pathway (5) leads to the emission of LMM -Auger electrons in our region of interest. This is corresponding to the green curve in Fig. 3, leading to Ar^{2+} ions. While the transition to $3p^4$ final states is accurately matched by the calculations, the transition to $3s^1 3p^5$ final states was found at slightly higher energy and with smaller splitting than calculated. Note that this is not the only possible decay channel terminating at doubly charged ions; KMM -Auger decay has been observed [59], too, with a decay probability of 0.4% [34]. Additionally, Ref. [53] reported double and triple Auger decay of the argon $2p^{-1}$ hole. However, the energies of the electrons emitted in these processes lie below that of our region of interest. In total, Ar^{2+} contributed 9.7% of all measured ions, in perfect agreement with the results of Ref. [36].

Radiative decay to more than triply charged ions is negligible [36]. Besides the above-mentioned multiple Auger processes, the main contribution to Ar^{3+} ions (blue curve in Fig. 3) is via KLM - (7) and LMM -Auger decay (8):

$$\gamma(3550 \text{ eV}) + \text{Ar} \rightarrow \text{Ar}^{1+}(1s^1) + e_{\text{ph}}^- (\approx 344 \text{ eV}), \quad (6)$$

$$\text{Ar}^{1+}(1s^1) \rightarrow \text{Ar}^{2+}(2p^5 3p^5) + e_{\text{Auger1}}^- (\approx 2920 \text{ eV}), \quad (7)$$

$$\text{Ar}^{2+}(2p^5 3p^5) \rightarrow \text{Ar}^{3+}(3p^3) + e_{\text{Auger2}}^- (\approx 195 \text{ eV}). \quad (8)$$

This process has a probability of 13.6% of the overall non-radiative decay after $1s$ ionization [36]. The electron emitted in Eq. (8) is one of the original reasons for performing our own calculations, since the calculations reported by Guillemin *et al.* differ considerably from the experimental results in structure and put the transition about 10 eV higher than measured [36].

The transition of Eq. (8) was further analyzed by Huttula *et al.* in Ref. [60], where more details can be found.

The dominant $\text{Ar}^{1+}(1s^{-1})$ decay path is $KL_{2,3}L_{2,3}$ -Auger decay, which constitutes 49.1% [56,58] of the overall decay of the $1s$ hole (including both radiative and nonradiative decay pathways). This decay path, which is discussed in detail in Sec. IV B, terminates at Ar^{4+} , which indeed contributes 49% of all ions we measure. This leads us to the assumption that virtually all quadruply charged ions in our experiment are created via KLL -Auger decay leading to $2p^{-2}$ DCH states, which further decay by emission of two Auger electrons. Our measured yield of 49% compares well to the 46% previously reported [36,61] and calculated [37].

We believe our Ar^{5+} signal to be contaminated by false coincidences at the only discernible structure at 200–220 eV, due to its close resemblance to the total spectrum. This structure was also not observed in Ref. [36], where all measured electrons lie below 190 eV. Furthermore, strong signal ringing is visible in our spectrum for energies below 180 eV. We thus omitted Ar^{5+} [gray curve in Fig. 3(b)] from our calculations, as well as the weak signals of Ar^{6+} (yellow curve) and Ar^{7+} (purple curve), which combined contribute 3% to the total ion yield, which is lower than the 6% reported by Ref. [36].

In conclusion, while coincidence filtering with respect to Ar^{4+} ions ensures that only decay of the DCH contributes electrons to the final data, no other decay pathway involves two correlated electrons in the correct range with any discernible structure. We can thus safely restrict filtering to threefold coincidences ($1s$ photoelectron plus two Auger electrons in the range 170–240 eV), resulting in better statistics than when additionally including ion filtering.

B. Decay of $\text{Ar}^{2+}(2p^{-2})$ double core holes

The DCHs are created via KLL -Auger decay after $1s$ ionization. The most populated $\text{Ar}^{2+}(2p^{-2})$ DCH level is the 1D_2 level, but also $^3P_{0,1,2}$ and 1S_0 are populated (with 1.2 and 13% probability, respectively, when normalized to the probability of decay to the 1D_2 state [32,62]). These levels then undergo further decay, dominantly via a cascade emitting two more Auger electrons (denoted by the subscripts A1 and A2):

$$\gamma(3550 \text{ eV}) + \text{Ar} \rightarrow \text{Ar}^{1+}(1s^1) + e_{\text{ph}}^- (\approx 344 \text{ eV}), \quad (9)$$

$$\begin{aligned} \text{Ar}^{1+}(1s^1) \rightarrow \text{Ar}^{2+}(2p^4) + e_{\text{KLL}}^- \\ \times [\approx 2660.5 \text{ eV}(^1D_2)(\text{see Ref. [32]})], \end{aligned} \quad (10)$$

$$\begin{aligned} \text{Ar}^{2+}(2p^4) \rightarrow \text{Ar}^{3+}(2p^5 3p^4) + e_{\text{A1}}^- (\approx 210 - 230 \text{ eV}), \\ \text{Ar}^{3+}(2p^5 3p^4) \rightarrow \text{Ar}^{4+}(3p^2) + e_{\text{A2}}^- (\approx 175 - 190 \text{ eV}). \end{aligned} \quad (11)$$

Alternatively, Eqs. (11) and (12) can involve one or two $3s$ holes:

$$\begin{aligned} \text{Ar}^{2+}(2p^4) \rightarrow \text{Ar}^{3+}(2p^5 3s^1 3p^5) + e_{\text{A1}}^- (\approx 195 - 230 \text{ eV}), \\ \text{Ar}^{3+}(2p^5 3s^1 3p^5) \rightarrow \text{Ar}^{4+}(3s^1 3p^3), (3s^0 3p^4) \\ + e_{\text{A2}}^- (\approx 170 - 190 \text{ eV}). \end{aligned} \quad (12)$$

The creation and decay of the DCHs is schematically shown in Fig. 1, including the branching ratios of the $2p^{-2}$ levels. The dominant decay pathway [Eqs. (11)–(14)] to Ar^{4+} final states is shown in red. The other two possible decay pathways, the weak decay to Ar^{3+} ions and the potentially possible but not successfully measured decay to Ar^{3+} ions, are further discussed in Sec. IV C. The main $2p^{-2}$ level, 1D_2 , has a binding energy of ≈ 545.75 eV, as given by subtracting the kinetic energy of the Auger electron from the $1s$ binding energy (also see Ref. [63]). Note that this value is slightly at odds with the results of Ref. [64], who created the DCH levels by double photon ionization and measured a binding energy of 546.9 eV.

The spectrum of the electrons emitted by processes (11)–(14) is given by the red trace in Fig. 3. The lower-energy part up to 190 eV corresponding to the second Auger step of the cascade [Eqs. (12) and (14)] agrees well with theory. However, for those transitions of Eq. (13) that fall into the kinetic-energy range 195–210 eV, the splitting has been overestimated by the calculations. Furthermore, the calculated first step of the Auger cascade at an energy of 215–230 eV is shifted by about 5 eV to higher energies in comparison to the experimental results. For assignment, we aligned the calculations with respect to the most intense line at 216.28 eV (Table I).

Previous calculations performed for XFEL experiments [38] predicted an energy range for the first [Eqs. (11) and (13)] and second Auger electron [Eqs. (12) and (14)] of 181–241 and 140–198 eV, respectively, and thus an overlap in the energy range 181–198 eV. Our results of 195–230 and 170–190 eV do not confirm this overlap for any transition of significant intensity. According to Ref. [38], when an Auger electron is measured in the kinetic-energy range 208–241 eV (even in a single electron spectrum without applying coincidence techniques), that is sufficient evidence for the occurrence of a $2p^{-2}$ DCH.

However, to gain further insight into the dynamics of the decay of the DCHs, and to analyze the intermediate states, we constructed a two-dimensional coincidence map (Fig. 4), correlating the two subsequent Auger electrons e_{A1} and e_{A2} , with e_{A1} on the horizontal axis and e_{A2} on the vertical axis. The coincidence map shows “island” structures, corresponding to the individual (two-step) decay pathways. Importantly, we can distinguish between decay from $2p^{-2} {}^1D_2$ and 1S_0 because the binding-energy difference of the two levels of 9.6 eV [32] leads to an equal shift in *kinetic* energy of the first emitted Auger electron e_{A1} . Because a kinetic energy of e_{A1} of 223 eV corresponds to decay from $2p^{-2} {}^1D_2$ to the Ar^{3+} ground state, any transition with higher kinetic energy can safely be assigned to decay from $2p^{-2} {}^1S_0$. However, this is the only energy region for which this separation is safely possible. The other parts of the coincidence map could show contributions from both initial $2p^{-2}$ levels, but since 1D_2 is the most strongly populated by a factor of 8, this level can in first approximation be seen as the sole contributor (hence the labeling). The $2p^{-2} {}^3P$ levels were too weakly populated to be measured.

To further disentangle the region where overlap between the decay of the levels happens, theoretical calculations were necessary. Because the energy of e_{A1} [Eqs. (11) or (13)] is generally smaller than that of e_{A2} [Eqs. (12) or (14)], we can consider projections on the horizontal axis of Fig. 4 to reveal Ar^{3+} intermediate states. The results of both calculations and experiment are given in Fig. 5 and Table II, in binding energy. Note that the axis is reversed to allow for easier comparison with the preceding figures given in kinetic energy. The experimental spectrum is separated into decay from the different $2p^{-2}$ levels only where possible (the cutoff in the spectrum for $2p^{-2} {}^1S_0$ corresponds to the above-mentioned 223-eV kinetic energy, beyond which the black curve shows dominantly, but not exclusively, decay from $2p^{-2} {}^1D_2$). The calculations suggest a strong difference between decay from the different DCH states; however, this

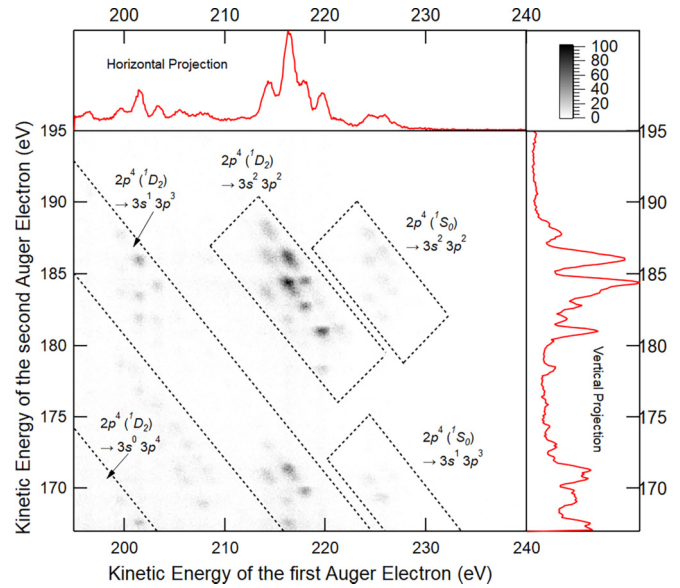


FIG. 4. Two-dimensional map showing three particle coincidences between the $1s$ photoelectron and the two Auger electrons of Eqs. (11) and (12), or Eqs. (13) and (14). The projection on the horizontal axis gives the kinetic energy of the first Auger electron [Eqs. (11) and (13)], and the vertical projection gives that of the following Auger electron [Eqs. (12) and (14)]. The Ar^{4+} final states’ histogram is given by the sum of the kinetic energy of the Auger electrons (see Fig. 7). The most prevalent decay pathways are marked by boxes of dashed lines, the most intense one leading from $2p^4 {}^1D_2$ to $3s^2 3p^2$, others being $2p^4 {}^1D_2$ to $3s^1 3p^3$ or $3s^0 3p^4$, and $2p^4 {}^1S_0$ to $3s^2 3p^2$ or $3s^1 3p^3$. The states which are visible in the figure but are not labeled (most notably at $\sum E \approx 385$ eV) belong to satellite transitions leading to final states of the form $3s^2 3p^1 nl^1$ that we do not study further in this paper. The employed color scale is linear.

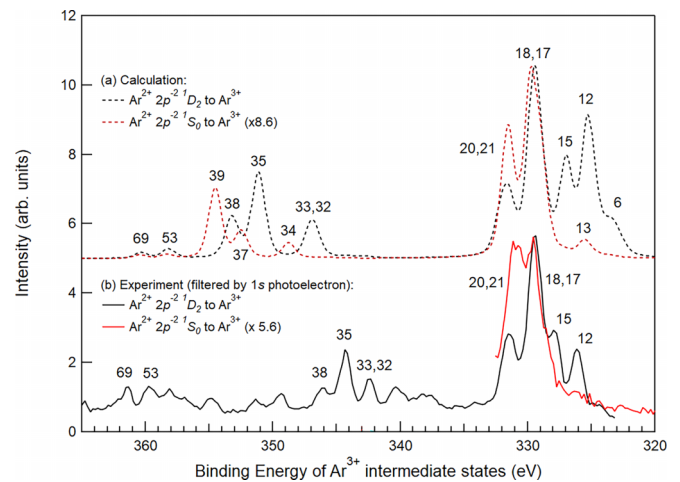


FIG. 5. The Ar^{3+} intermediate states, which decay further to the Ar^{4+} final states shown in Fig. 7. The experimental results are shown in black (decay from $2p^{-2} {}^1D_2$) and red (from $2p^{-2} {}^1S_0$); the dashed black (from $2p^{-2} {}^1D_2$) and dashed red curves (from $2p^{-2} {}^1S_0$) are the calculated results. The alignment between theory and calculation was done with respect to the most intense peak at 329.47 eV. The correspondence is good enough to allow for the assignment of involved states. The labeled peaks refer to Table II, where precise binding energies are listed.

TABLE I. The kinetic energies (KE) of the Auger electrons of the transition $2p^{-2}(^1D_2 \text{ or } ^1S_0) \rightarrow (2p^5 3s^2 3p^4 + 2p^5 3s^1 3p^5 + 2p^5 3s^0 3p^6)$ are listed with the relative transition rates given in terms of percent of the dominant transition at 216.28 eV. The intensities for all possible transitions were calculated and labeled numerically. However, the contributions with less than 0.5% intensity and those outside the selected energy range (180–240 eV) have been omitted, except when their counterpart from the other starting configuration leads to a transition with significant intensity. Identical labels for the different starting configurations 1D_2 and 1S_0 refer to transitions to the same state. The most prominent experimental peaks are given for comparison. Entries marked by an asterisk (*) are not fully confirmable.

Configuration		Label	$2J$	Calc. KE (eV)	I (a.u.)	Expt. KE (eV)	I (a.u.)	
$2p^4 \ ^1D_2 \rightarrow$	$2p^5 3s^2 3p^4$	1	1	224.16	0.0			
		3	5	223.12	2.8			
		4	5	222.80	6.0			
		5	3	222.63	3.1			
		6	3	222.25	13.9			
		7	1	222.15	2.3			
		8	3	221.41	5.7			
		9	5	221.31	8.4			
		11	1	220.60	5.6			
		12	7	220.46	89.3	219.60	28.7	
		13	3	220.26	10.1			
		14	3	219.02	2.9			
		15	5	218.74	69.2	217.90	30.3	
		16	3	216.94	31.0			
		17	5	216.28	100.0	216.28	100.0	
	18	1	216.06	1.2				
	19	3	216.05	37.3				
	20	3	214.29	37.0				
	21	1	213.65	29.1	214.21	42.0		
	$2p^5 3s^1 3p^5$	23	5	203.06	1.0			
		27	3	201.54	0.9			
		29	5	201.04	0.5			
		31	3	199.81	0.6			
		32	3	199.00	15.7			
		33	5	198.62	16.3	203.35	16.3	
		35	5	194.62	63.4	201.58	34.0	
		36	3	194.20	5.6			
		38	3	192.50	31.8	199.57	13.3	
		$2p^5 3s^0 3p^6$	53	3	187.51	7.2	186.12	11.4
			69	1	185.37	4.5	184.40	5.2
	$2p^4 \ ^1S_0 \rightarrow$	$2p^5 3s^2 3p^4$	12	7	230.06	0.6		
			13	3	229.86	1.7		
15			5	228.34	0.6			
16			3	226.54	12.4			
17			5	225.88	0.1			
18			1	225.66	18.5	225.70	13.8	
19			3	225.65	6.8			
20			3	223.89	19.5	224.26	8.5	
21			1	223.25	0.0			
$2p^5 3s^1 3p^5$		34	1	206.67	2.3			
		35	5	204.22	0.0			
		37	1	202.95	4.1			
		39	1	200.91	10.9	208.31*	4.9*	
$2p^5 3s^0 3p^6$		53	3	197.11	0.5			
		69	1	194.97	0.5			

difference is most strongly pronounced in the region beyond where we can clearly separate decay from 1S_0 and 1D_2 . Further, the calculations do not match the experiment well in this region, shifting the structure of states 32–39 by about 5 eV (see Tables I and II for the labels) and overestimating the splitting. These states are of the configuration $2p^5 3s^1 3p^5$

and thus contain three open shells. For these systems, our calculations apparently do not take electron correlation into account, properly. To safely establish the difference in decay from the two $2p^{-2}$ levels, we thus concentrate on the region where we can achieve a clear experimental distinction, i.e., 320–333-eV binding energy. In this region, the states 6 and 13

TABLE II. The binding energies (BE) of the intermediate Ar^{3+} states reached by the transitions listed in Table I. The listed experimental binding-energy values follow by subtracting the Auger electrons from Table I from the binding energy of the DCHs, which are 545.75 eV for $2p^{-2} \ ^1D_2$ and 555.35 eV for $2p^{-2} \ ^1S_0$, respectively (via subtracting the *KLL*-Auger electron's energy from the 1s ionization energy [63]). Entries marked by an asterisk (*) are not fully confirmable.

Configuration	Label	Calc. $2J$	Expt. BE (eV)	BE (eV)
$2p^5 3s^2 3p^4$	1	1	321.59	
	3	5	322.63	
	4	5	322.95	
	5	3	323.12	
	6	3	323.50	
	7	1	323.60	
	8	3	324.34	
	9	5	324.44	
	11	1	325.15	
	12	7	325.29	326.15
	13	3	325.49	
	14	3	326.73	
	15	5	327.01	327.85
	16	3	328.81	
	17	5	329.47	329.47
	18	1	329.69	329.65
	19	3	329.70	
	20	3	331.46	331.09
	21	1	332.10	331.54
$2p^5 3s^1 3p^5$	23	5	342.69	
	27	3	344.21	
	29	5	344.71	
	31	3	345.94	
	32	3	346.75	
	33	5	347.13	342.40
	34	1	348.68	
	35	5	351.13	344.17
	36	3	351.55	
	37	1	352.40	
38	3	353.25	346.18	
39	1	354.44	347.04*	
$2p^5 3s^0 3p^6$	53	3	358.24	359.63
	69	1	360.38	361.35

(see Table II for the numerical labels) are predicted with weak intensity but could not be observed. The states 12 and 15 were measured only in case of decay from $2p^{-2} \ ^1D_2$, confirming our calculations despite the overestimation in intensity. For the following two lines, observed at 329–330 and 330–332 eV, respectively, it cannot immediately be decided to which states they correspond. However, the calculations suggest decay from $2p^{-2} \ ^1D_2$ to state 17 and to a mixture of states 20 and 21, while $2p^{-2} \ ^1S_0$ decays to state 18 and 20. We cannot resolve these states experimentally, but if both $2p^{-2}$ levels indeed decay to different Ar^{3+} states, their further decay to Ar^{4+} final states is expected to differ as well. This, however, can be experimentally verified by measuring the final states in coincidence with different intermediate states that differ in

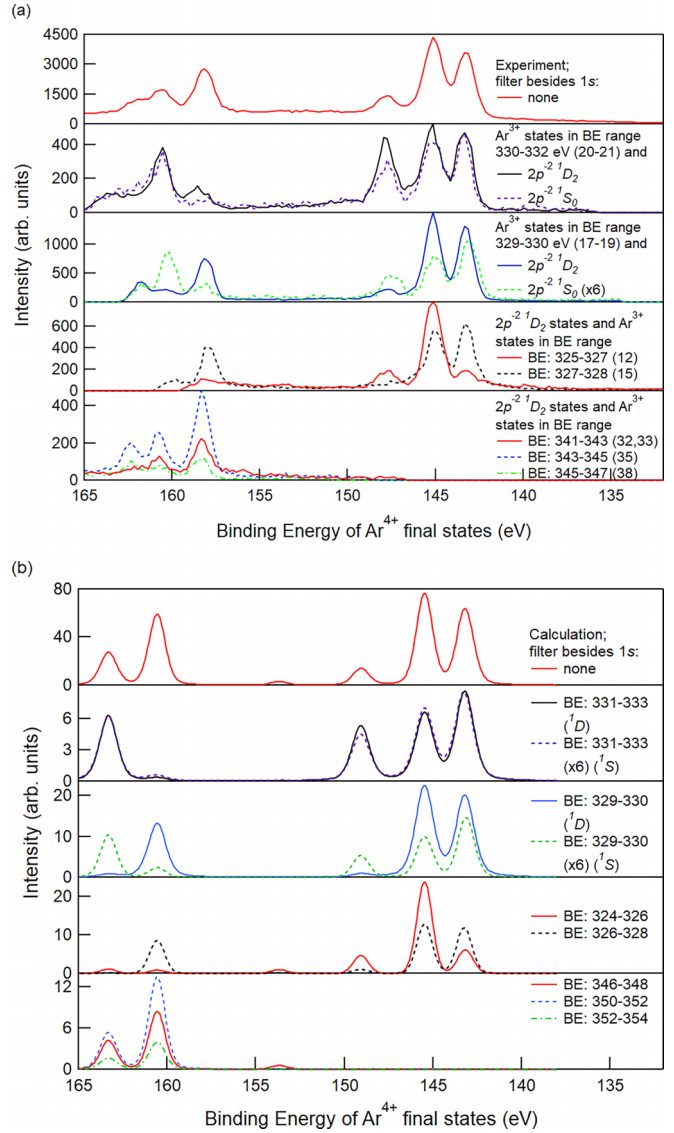


FIG. 6. (a) Experimental spectra of Ar^{4+} final states originating from different initial DCH and in coincidence with Ar^{3+} intermediate states. The given numerical labels (in parentheses) correspond to the main states of each filtered binding-energy range, as listed in Table II. (b) Corresponding calculated spectra.

kinetic energies of e_{A1} . The result is given in Fig. 6 in binding energies together with the calculations. The first two panels reveal that the further decay of the two unresolved Ar^{3+} lines is dependent on whether they are populated by decay from $2p^{-2} \ ^1S_0$ or 1D_2 , establishing that indeed different Ar^{3+} intermediate states are populated. That these unresolved lines are separate states was previously suggested in Ref. [56] and can hereby be confirmed. Further, since the calculations reproduce the decay to Ar^{4+} final states correctly, we can safely assign the measured lines: $2p^{-2} \ ^1D_2$ decays mostly to state number 17 (experimental binding energy of 329.47 eV) and a mixture of states 20 and 21 (331.54 eV). The 1S_0 DCH on the other hand does not decay to the states 17 and 21 at all, rather to the neighboring states 18 (329.65 eV) and 20 (331.09 eV). The calculations also reproduce the decay of states 12

and 15 (solely populated by 1D_2) well, confirming the assignment.

Regarding the region beyond 333-eV binding energy, the weak states 34 and 37, which would reveal decay from $2p^{-2} ^1S_0$, could not be measured. The further decay of the lines measured at 342.40, 344.17, and 346.18 eV agrees well with the calculated decay of the states 32 and 33, 35, and 38, respectively, and can thus be assigned. While the states 36 and 37 also contribute to this region, their calculated intensity is small. State 39, which is only populated by decay from $2p^{-2} ^1S_0$, is potentially seen at 208.31-eV kinetic energy in Fig. 4. This assignment is supported by the calculations of Ref. [56] (resulting in 208.47 eV) and would lead to a wrong binding energy in Fig. 5 (347.04 eV in Fig. 5, 337.44 eV if the assignment as state 39 is correct), because we cannot properly separate decay from the different DCH levels for this energy. However, our calculations differ strongly from the experimental results here, and the state was not measured by Ref. [56]. Hence, the assignment remains doubtful. The states 53 and 69, with a configuration of $2p^5 3s^0 3p^6$, could be measured and agree well with theory. The states that are not labeled in Fig. 5 could not be assigned safely. Decay involving shake-up satellite states could potentially contribute to this region, as well.

In addition to the partial yield of Ar^{4+} final states after decay of the individual states discussed above, the full histogram of final states is given by integrating Fig. 4 along diagonal lines with the same kinetic-energy sum. The binding energy then results from subtraction of this sum of kinetic energies of e_{A1} and e_{A2} from the binding energy of $2p^{-2}$. The results are given in Fig. 7 and Table III. There, the red line only indicates states populated by decay of those Ar^{3+} intermediate states that could clearly be identified as belonging to decay from $2p^{-2} ^1S_0$, while the black line corresponds to decay from all other levels. The black line could thus include contributions from $2p^{-2} ^1S_0$; however, those are expected to be small because $2p^{-2} ^1D_2$ is more strongly populated. Additionally, up to 150 eV the separation between decay from the two DCH levels is clear and complete, because decay to final states with low binding energies involves emittance of electrons with high kinetic energies, which can clearly be assigned, as discussed above.

Binding energies of the Ar^{4+} electronic states are found in the NIST database [65]. A shift of -0.5 eV between the NIST values and our experimental results was found (see Fig. 7). This is essentially caused by a small difference in the Ar^{4+} ground-state energy, which the NIST table lists at (143.704 ± 0.196) eV [66], while we measure (142.99 ± 0.50) eV. The NIST values stem from measurements of the neutral [67] and singly charged atom [68], and Dirac-Fock calculations for the following charge states [69,70]. We note that von Busch *et al.* [56] reported a similar discrepancy. They experimentally obtained (143.04 ± 0.33) eV for the Ar^{4+} ground state, which is in agreement neither with the NIST values given at their time of writing (143.94 eV [71]) nor with the most recent values we refer to above. However, the values by von Busch *et al.* are in good agreement with our experimentally obtained binding energy of the ground state. Our calculation (aligned with the experiment by setting the energy of state 3 in Table III to 143.23 eV) reproduces the observed states

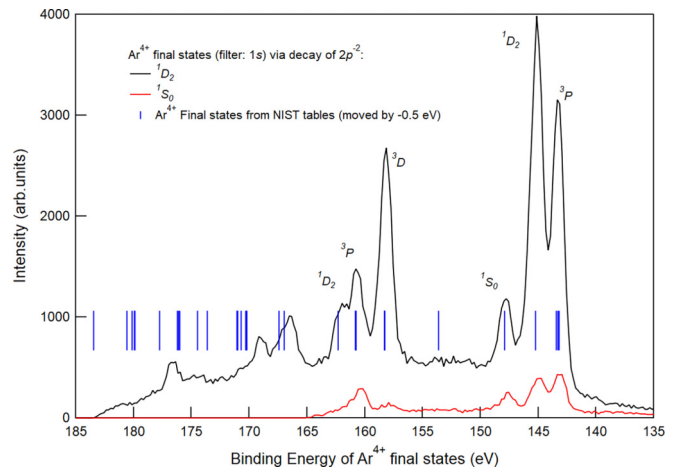


FIG. 7. The final electronic states of the decay of argon $2p^{-2}$ double core holes. The binding energy was found by subtracting the energies of the two Auger electrons from Fig. 4 from the binding energy of the $2p^{-2}$ DCH. The difference in binding energy between $2p^{-2} ^1S_0$ and 1D_2 is 9.6 eV [32]. The final states reached via decay from these two different levels are shown separately in the graph. The energy of the states is compared to those given by the NIST [65] database. This way the states could be assigned, which is exemplarily done in this figure for the six most intense peaks, of which the first three at lowest binding energy (3P , 1D , and 1S) have a leading configuration of $3s^2 3p^2$, and the next three (3D , 3P , and 1D) have a leading configuration of $3s^1 3p^3$. A complete list of the final states is given in Table III. Note the shift of -0.5 eV between the (calculated) NIST values and the experimental values.

with reasonable accuracy. However, there is a big energy discrepancy regarding state 13, with the calculations differing from the measurements by more than 5 eV. Generally, most reasonably separated final states could be measured, even in the case of small intensities. However, states separated by less than 0.5 eV could not be distinguished due to resolution. Thus, the different levels of, e.g., $\text{Ar}^{4+}(3s^2 3p^2 ^3P)$ could not be individually measured. Another state causing difficulty is the state measured at 176.66 eV. The NIST tables and our calculation indicate a 3P configuration, while von Busch's calculations imply a 1D_2 configuration [56].

The analysis above would have not been possible without calculations and the coincidence experiments to which to compare them. While previous works [56] have shown similar calculations, they could only compare them to the total electron spectrum, which prevents a full analysis. Additionally, while in case of the work of von Busch *et al.* [56] the calculations seem very precise, they are apparently done by placing each set of states separately in terms of binding energy, which is justified by their desire to assign the previously unassigned states. To make a further analysis possible, however, we calculated the splitting between each contribution instead and only aligned the whole set with respect to the experiment without shifting the different contributions relative to each other.

C. Further decay pathways involving $2p^{-2}$ double core holes

Besides the dominant decay to Ar^{4+} , the DCHs can also decay via an interesting two-electron-one-electron (TEOE) conversion, described in detail by Žitnik *et al.* [62] and given

TABLE III. The binding energies (BE) of the final Ar^{4+} states reached after decay of the DCH. The results of our calculations are compared to the values given by the NIST database [65] and to the experimental results. The term symbols and $2J$ values are listed. The difference between the NIST values and the experimental values of the present paper (especially in the low-binding-energy range, which includes the most intense states; see Fig. 7) is mostly due to the difference in the ground state of the NIST values; see Sec. IV B. The alignment of the calculations in binding energy has been done with respect to the measured $3s^2 3p^2 \ ^3P_2$ level at 143.23 eV.

Configuration	Label	$2J$	Term	Calc. BE (eV)	[65]	Expt. BE (eV)
$3s^2 3p^2$	1	0	3P_0	142.99	143.70	
	2	2	3P_1	143.08	143.80	
	3	4	3P_2	143.23	143.96	143.23
	4	4	1D_2	145.45	145.72	145.09
	5	0	1S_0	149.04	148.40	147.76
$3s^1 3p^3$	6	4	5S_2	153.65	154.13	
	7	2	3D_1	160.53	158.78	
	8	4	3D_2	160.53	158.79	
	9	6	3D_3	160.54	158.81	158.14
	10	4	3P_2	163.29	161.28	160.59
	11	2	3P_1	163.28	161.28	
	12	0	3P_0	163.27	161.30	
	13	4	1D_2	167.54	162.82	161.93
$3s^0 3p^4$	14	2	3S_1	167.70	167.45	166.59
	15	2	1P_1	170.44	167.93	169.01
	16	4	3P_2	175.72	176.49	176.66 ^a
	17	2	3P_1	176.86	176.63	
	18	0	3P_0	176.92	176.69	
	19	4	1D_2	177.37	178.24	
	20	0	1S_0	182.63	183.98	

^aThe assignment of this state is not entirely clear; see Sec. IV B.

by the blue line in Fig. 1. The decay path is as follows (see Fig. 8):

$$\gamma(3550 \text{ eV}) + \text{Ar} \rightarrow \text{Ar}^+(1s^1) + e_{\text{ph}}^-(\approx 344 \text{ eV}), \quad (15)$$

$$\text{Ar}^+(1s^1) \rightarrow \text{Ar}^{2+}(2p^4) + e_{\text{Auger1}}^-(\approx 2660.5 \text{ eV})$$

[*KLL*-Auger decay (see Ref. [32])], \quad (16)

$$\text{Ar}^{2+}(2p^4) \rightarrow \text{Ar}^{3+}(3p^3) + e_{\text{Auger2}}^-(458.5 \text{ eV}). \quad (17)$$

Here, the DCH gets simultaneously filled by two electrons while the residual energy leaves the atom via a single Auger electron of (458.5 ± 1.0) -eV kinetic energy (main transition; this agrees very well with the 458.65 eV found by Ref. [62]), leading to $\text{Ar}^{3+}(3p^3)$ final states. The emitted Auger electron is well separated in energy from all other observed electrons and can thus be observed despite the transition's small cross section. The measured spectrum is shown in Fig. 8.

The probability of the TEOE decay P_{TEOE} is given by the following quotient:

$$P_{\text{TEOE}} = \frac{A(\text{Ar}^{3+}, 458.5 \text{ eV}) P_{\text{el}}(200 \text{ eV}) P_{\text{ion}}(\text{Ar}^{4+})}{\frac{1}{2}A(\text{Ar}^{4+}, 180 - 240 \text{ eV}) P_{\text{el}}(455 \text{ eV}) P_{\text{ion}}(\text{Ar}^{3+})}. \quad (18)$$

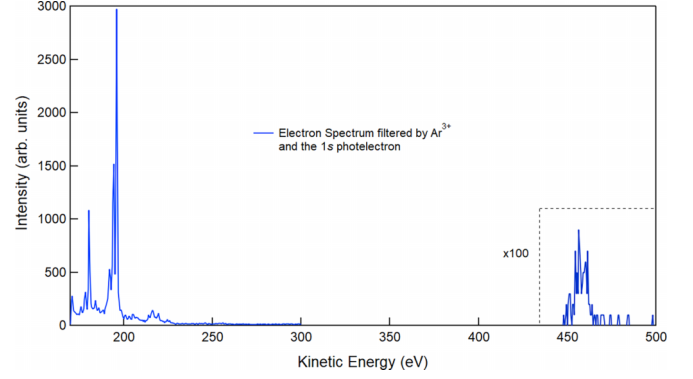


FIG. 8. Electron spectrum filtered by the Ar^{3+} ion and the $\text{Ar}^{1+}(1s)$ photoelectron. The two-electron–one-electron conversion [62] is found in the dashed box (same kinetic-energy scale as the overall graph, but intensity scaled by a factor of 100) at (458.5 ± 1.0) eV (previously reported, 458.65 eV; see Ref. [62]). The region 300–350 eV is omitted due to false coincidences caused by overlap with the satellite of the $1s$ photoelectron that were left even after filtering with respect to $1s$ photoemission.

Here, A indicates the area under the spectrum, while P_{el} and P_{ion} are the detection efficiencies of the electrons and ions, respectively. The electron detection efficiencies have to be included in Eq. (18), because the TEOE process involves electrons that are significantly faster (and thus harder to detect) than the Auger electrons emitted in decay to Ar^{4+} final states. The result of $1.9 \times 10^{-3} \pm 1.0 \times 10^{-3}$ compares well to the theoretical estimate of 1.4×10^{-3} given by Ref. [62], and their experimental result of 2.2×10^{-3} .

While coincidences with Ar^{5+} ions could be measured for the $K-L_1-L_3$ (at 2599.7 eV [32]) and $K-L_{2,3}-L_{2,3}$ Auger transitions, the statistics were too low to assert the subsequent decay paths with certainty. It has been previously suggested that the main process creating five times charged ions leads from $\text{Ar}^{2+}(2s^1 2p^5)$ states via single Auger filling of the $2p$ hole and double Auger filling of the $2s$ hole to Ar^{5+} final states [35]. We cannot confirm this pathway here. However, we can say with certainty that further decay to Ar^{5+} or higher of the states mentioned in Sec. IV B is not possible because they lie below threshold (219-eV binding energy [65]; see Fig. 7, where the highest measured binding energy is about 185 eV). To our knowledge, no pathway including the $2p^{-2}$ DCH leading to Ar^{5+} final states has been detected. Furthermore, according to Muller *et al.* [27], the cross section of fivefold photoionization of Ar^+ was found to become important when $2s 2p$ or $2s 2s$ double-core-hole states are energetically available.

V. SUMMARY

The full set of decay pathways following $1s$ ionization of argon has been measured and compared to theory to very good agreement. Electron-ion coincidences allowed us to separate the final states by ionic charge. The dominant pathway has been found to lead to quadruply charged final states (49% of all decay pathways).

Decay processes following $\text{Ar}^{2+}(2p^{-2})$ DCH intermediate states have been isolated and analyzed in detail. The decay of

this L shell DCH has been found to lead to Ar^{3+} ($3p^3$) final states with a decay probability of 1.9×10^{-3} , otherwise to Ar^{4+} final states.

The former of these two decay pathways involves a two-electron–one-electron transition with a single Auger electron emitted with a kinetic energy of 458.5 eV. The findings agree very well with previously published work [62].

The dominant decay pathway of the DCHs leading to Ar^{4+} final states have been studied both in terms of intermediate- and final-state energies and intensities. Importantly, the different $2p^{-2}$ levels, 1S_0 and 1D_2 , lead to a different population of intermediate and final states. The states have been assigned by comparison to theory. A small discrepancy of -0.5 eV to the (theoretical) Ar^{4+} ground state of the NIST reference table [65] has been found.

This paper demonstrates the advantage of the chosen method in disentangling processes that are strongly overlapping in kinetic energy of the emitted electrons. This approach allows us to compare selected subsets to theory instead of comparing the overall spectrum and makes it possible to compare decay from the different $2p^{-2}$ levels. Furthermore,

the technical difficulties in creating DCH states have been circumvented by using an atom with dominant decay to an L shell double core hole after $1s$ ionization. This enabled the use of a synchrotron radiation source and thus a multicoincidence setup. The used method is generally applicable to a wide range of atoms and molecules. Especially molecules isoelectronic to argon, such as HCl, could be an interesting target for further study, employing the same method as published here.

ACKNOWLEDGMENTS

M.M., M.H., and M.P. acknowledge funding by the Academy of Finland. F.H. acknowledges funding from the European Union’s Horizon 2020 research and innovation program under Marie Skłodowska-Curie Grant No. 792676, and R.F. acknowledges funding from the Swedish Research Council and the Knut and Alice Wallenberg Foundation, Sweden. Experiments were carried out at the GALAXIES beamline with the approval of Synchrotron SOLEIL (Proposal No. 20181467). We thank J. P. Rueff and D. Prieur from the GALAXIES beamline for their technical support.

-
- [1] G. Charpak, Experimental study of the double ionization of the K shell of 55Mn in the disintegration of 55Fe by K-capture, *C. R. Acad. Sci.* **237**, 243 (1953).
- [2] J. Hoszowska, J. C. Dousse, W. Cao, K. Fennane, Y. Kayser, M. Szlachetko, J. Szlachetko, and M. Kavčič, Double K-shell photoionization and hypersatellite x-ray transitions of $12 \leq Z \leq 23$ atoms, *Phys. Rev. A* **82**, 063408 (2010).
- [3] L. S. Cederbaum, F. Tarantelli, A. Sgamellotti, and J. Schirmer, On double vacancies in the core, *J. Chem. Phys.* **85**, 6513 (1986).
- [4] P. Lablanquie *et al.*, Properties of Hollow Molecules Probed by Single-Photon Double Ionization, *Phys. Rev. Lett.* **106**, 063003 (2011).
- [5] M. Nakano *et al.*, Single Photon K^{-2} and $K^{-1}K^{-1}$ Double Core Ionization in C_2H_2n ($N = 1-3$), CO, and N₂ As a Potential New Tool for Chemical Analysis, *Phys. Rev. Lett.* **110**, 163001 (2013).
- [6] L. Hedin, M. Tashiro, P. Linusson, J. H. D. Eland, M. Ehara, K. Ueda, V. Zhaunerchyk, L. Karlsson, K. Pernestål, and R. Feifel, N_{1s} and O_{1s} double ionization of the NO and N₂O molecules, *J. Chem. Phys.* **140**, 44309 (2014).
- [7] M. Tashiro, M. Nakano, M. Ehara, F. Penent, L. Andric, J. Palaudoux, K. Ito, Y. Hikosaka, N. Kouchi, and P. Lablanquie, Auger decay of molecular double core-hole and its satellite states: Comparison of experiment and calculation, *J. Chem. Phys.* **137**, 224306 (2012).
- [8] S. Carniato *et al.*, Double-core ionization photoelectron spectroscopy of C₆H₆: Breakdown of the “intuitive” ortho-meta-para binding energy ordering of $K^{-1}K^{-1}$ states, *J. Chem. Phys.* **151**, 214303 (2019).
- [9] S. Carniato *et al.*, Single photon simultaneous K-shell ionization/excitation in C₆H₆: experiment and theory, *J. Phys. B* **53**, 244010 (2020).
- [10] L. S. Cederbaum, F. Tarantelli, A. Sgamellotti, and J. Schirmer, Double vacancies in the core of benzene, *J. Chem. Phys.* **86**, 2168 (1987).
- [11] F. Penent *et al.*, Double core hole spectroscopy with synchrotron radiation, *J. Electron. Spectros. Relat. Phenom.* **204**, 303 (2015).
- [12] P. Lablanquie, F. Penent, and Y. Hikosaka, Multi-electron coincidence spectroscopy: Double photoionization from molecular inner-shell orbitals, *J. Phys. B* **49**, 182002 (2016).
- [13] M. Nakano, P. Selles, P. Lablanquie, Y. Hikosaka, F. Penent, E. Shigemasa, K. Ito, and S. Carniato, Near-Edge X-Ray Absorption Fine Structures Revealed in Core Ionization Photoelectron Spectroscopy, *Phys. Rev. Lett.* **111**, 123001 (2013).
- [14] S. Carniato *et al.*, Single photon simultaneous K-shell ionization and K-shell excitation. I. Theoretical model applied to the interpretation of experimental results on H₂O, *J. Chem. Phys.* **142**, 014307 (2015).
- [15] S. Carniato *et al.*, Single photon simultaneous K-shell ionization and K-shell excitation. II. Specificities of hollow nitrogen molecular ions, *J. Chem. Phys.* **142**, 014308 (2015).
- [16] S. Carniato *et al.*, Photon-energy dependence of single-photon simultaneous core ionization and core excitation in CO₂, *Phys. Rev. A* **94**, 013416 (2016).
- [17] L. Journel, D. Cubaynes, J.-M. Bizau, S. Al Moussalami, B. Rouvellou, F. J. Wuilleumier, L. VoKy, P. Faucher, and A. Hibbert, First Experimental Determination and Theoretical Calculation of Partial Photoionization Cross Sections of Lithium over the Energy Region of Hollow Atomic States, *Phys. Rev. Lett.* **76**, 30 (1996).
- [18] S. Diehl *et al.*, Hollow-atom-hollow-ion decay routes of triply excited lithium: First Auger results and a comparison with R-matrix calculations, *J. Phys. B* **30**, L595 (1997).

- [19] S. Diehl, D. Cubaynes, J. M. Bizau, F. J. Wuilleumier, E. T. Kennedy, J. P. Mosnier, and T. J. Morgan, New high-resolution measurements of doubly excited states of Li^+ , *J. Phys. B* **32**, 4193 (1999).
- [20] L. M. Kiernan, E. T. Kennedy, J.-P. Mosnier, J. T. Costello, and B. F. Sonntag, First Observation of a Photon-Induced Triply Excited State in Atomic Lithium, *Phys. Rev. Lett.* **72**, 2359 (1994).
- [21] G. Goldsztejn *et al.*, Double-Core-Hole States in Neon: Lifetime, Post-Collision Interaction, and Spectral Assignment, *Phys. Rev. Lett.* **117**, 133001 (2016).
- [22] G. Goldsztejn *et al.*, Experimental and theoretical study of the double-core-hole hypersatellite Auger spectrum of Ne, *Phys. Rev. A* **96**, 012513 (2017).
- [23] R. Püttner *et al.*, Argon $1s^{-2}$ Auger hypersatellites, *J. Phys. B* **54**, 024001 (2020).
- [24] D. Koulentianos *et al.*, KL double core hole pre-edge states of HCl, *Phys. Chem. Chem. Phys.* **20**, 2724 (2018).
- [25] A. Perry-Sassmannshausen *et al.*, Multiple Photodetachment of Carbon Anions Via Single and Double Core-Hole Creation, *Phys. Rev. Lett.* **124**, 083203 (2020).
- [26] S. Schippers, A. Hamann, A. Perry-Sassmannshausen, T. Buhr, A. Müller, M. Martins, S. Reinwardt, F. Trinter, and S. Fritzsche, Multiple photodetachment of oxygen anions via K-Shell excitation and ionization: direct double-detachment processes and subsequent deexcitation cascades, *Phys. Rev. A* **106**, 013114 (2022).
- [27] A. Müller, M. Martins, A. Borovik, T. Buhr, A. Perry-Sassmannshausen, S. Reinwardt, F. Trinter, S. Schippers, S. Fritzsche, and A. S. Kheifets, Role of L -Shell Single and Double Core-Hole Production and Decay in m -Fold ($1 \leq m \leq 6$) Photoionization of the Ar^+ Ion, *Phys. Rev. A* **104**, 033105 (2021).
- [28] N. Berrah *et al.*, Double-core-hole spectroscopy for chemical analysis with an intense x-ray femtosecond laser, *Proc. Natl. Acad. Sci. USA* **108**, 16912 (2011).
- [29] L. Young *et al.*, Femtosecond electronic response of atoms to ultra-intense x-rays, *Nature (London)* **466**, 56 (2010).
- [30] P. Salén *et al.*, Experimental Verification of the Chemical Sensitivity of Two-Site Double Core-Hole States Formed by an x-Ray Free-Electron Laser, *Phys. Rev. Lett.* **108**, 153003 (2012).
- [31] L. J. Frasinski *et al.*, Dynamics of Hollow Atom Formation in Intense X-Ray Pulses Probed by Partial Covariance Mapping, *Phys. Rev. Lett.* **111**, 073002 (2013).
- [32] L. Asplund, P. Kelfve, B. Blomster, H. Siegbahn, and K. Siegbahn, Argon KLL and KLM Auger electron spectra, *Phys. Scr.* **16**, 268 (1977).
- [33] G. Omar and Y. Hahn, Final charge state distribution in the production and decay of hollow Ar, *Z. Phys. D* **25**, 41 (1992).
- [34] R. Guillemin, C. Bomme, T. Marin, L. Journal, T. Marchenko, R. K. Kushawaha, N. Trcera, M. N. Piancastelli, and M. Simon, Complex decay patterns in atomic core photoionization disentangled by ion-recoil measurements, *Phys. Rev. A* **84**, 063425 (2011).
- [35] R. Guillemin, S. Sheinerman, C. Bomme, L. Journal, T. Marin, T. Marchenko, R. K. Kushawaha, N. Trcera, M. N. Piancastelli, and M. Simon, Ultrafast Dynamics in Postcollision Interaction after Multiple Auger Decays in Argon $1s$ Photoionization, *Phys. Rev. Lett.* **109**, 013001 (2012).
- [36] R. Guillemin *et al.*, Interplay of complex decay processes after argon $1s$ ionization, *Phys Rev A* **97**, 013418 (2018).
- [37] X. L. Wang, B. X. Liu, G. H. Zhang, P. Y. Wang, L. W. Liu, and X. Y. Li, Theoretical studies on the cascade decay processes of $1s$ -core-hole state of Ar ion, *J. Electron. Spectros. Relat. Phenom.* **250**, 147083 (2021).
- [38] A. O. G. Wallis, H. I. B. Banks, and A. Emmanouilidou, Traces in ion yields and electron spectra of the formation of Ar inner-shell hollow states by free-electron lasers, *Phys. Rev. A* **91**, 063402 (2015).
- [39] T. D. Thomas, Single and double core-hole ionization energies in molecules, *J. Phys. Chem. A* **116**, 3856 (2012).
- [40] J. P. Rueff, J. M. Ablett, D. Céolin, D. Prieur, T. Moreno, V. Balédent, B. Lassalle-Kaiser, J. E. Rault, M. Simon, and A. Shukla, The GALAXIES beamline at the SOLEIL synchrotron: Inelastic x-ray scattering and photoelectron spectroscopy in the hard x-ray range, *J. Synchrotron Radiat.* **22**, 175 (2015).
- [41] D. Céolin *et al.*, Hard x-ray photoelectron spectroscopy on the GALAXIES beamline at the SOLEIL synchrotron, *J. Electron. Spectros. Relat. Phenom.* **190**, 188 (2013).
- [42] J. H. D. Eland, O. Vieuxmaire, T. Kinugawa, P. Lablanquie, R. I. Hall, and F. Penent, Complete Two-Electron Spectra in Double Photoionization: The Rare Gases Ar, Kr, and Xe, *Phys. Rev. Lett.* **90**, 053003 (2003).
- [43] F. Penent, J. Palaudoux, P. Lablanquie, L. Andric, R. Feifel, and J. H. D. Eland, Multielectron Spectroscopy: The Xenon $4d$ Hole Double Auger Decay, *Phys. Rev. Lett.* **95**, 083002 (2005).
- [44] I. Ismail *et al.*, A modified magnetic bottle electron spectrometer for the detection of multiply charged ions in coincidence with all correlated electrons: Decay pathways to Xe^{3+} above xenon- $4d$ ionization threshold, *Phys. Chem. Chem. Phys.* **24**, 20219 (2022).
- [45] K. Ito, F. Penent, Y. Hikosaka, E. Shigemasa, I. H. Suzuki, J. H. D. Eland, and P. Lablanquie, Application of a simple asynchronous mechanical light chopper to multielectron coincidence spectroscopy, *Rev. Sci. Instrum.* **80**, 123101 (2009).
- [46] M. Breinig, M. H. Chen, G. E. Ice, F. Parente, B. Crasemann, and G. S. Brown, Atomic inner-shell level energies determined by absorption spectrometry with synchrotron radiation, *Phys Rev A* **22**, 520 (1980).
- [47] H. Pulkkinen, S. Aksela, O.-P. Sairanen, A. Hiltunen, and H. Aksela, Correlation effects in the $L_{2,3}$ -MM Auger transitions of Ar, *J. Phys. B: At. Mol. Opt. Phys.* **29**, 3033 (1996).
- [48] K. Bučar and M. Žitnik, Auger electron-ion coincidence spectrometry after electronic excitation of L -shell in argon, *Radiat. Phys. Chem.* **76**, 487 (2007).
- [49] M. F. Gu, The flexible atomic code, *Can. J. Phys.* **86**, 675 (2008).
- [50] K. G. Dyall, I. P. Grant, C. T. Johnson, F. A. Parpia, and E. P. Plummer, GRASP: A general-purpose relativistic atomic structure program, *Comput. Phys. Commun.* **55**, 425 (1989).
- [51] S. Fritzsche, C. F. Fischer, and G. Gaigalas, RELCI: A program for relativistic configuration interaction calculations☆☆this program can be downloaded from the CPC program library under catalogue identifier: <http://Cpc.Cs.Qub.Ac.Uk/Summaries/ADQH>, *Comput. Phys. Commun.* **148**, 103 (2002).
- [52] S. H. Southworth, T. LeBrun, Y. Azuma, and K. G. Dyall, Argon KM photoelectron satellites, *J. Electron. Spectros. Relat. Phenom.* **94**, 33 (1998).

- [53] P. Lablanquie, L. Andric, J. Palaudoux, U. Becker, M. Braune, J. Vieffhaus, J. H. D. Eland, and F. Penent, and Multielectron spectroscopy: Auger decays of the argon 2p hole, *J. Electron. Spectros. Relat. Phenom.* **156**, 51 (2007).
- [54] R. Püttner *et al.*, Argon *KLL* Auger spectrum: Initial states, core-hole lifetimes, shake, and knock-down processes, *Phys. Rev. A* **102**, 052832 (2020).
- [55] M. O. Krause, Atomic radiative and radiationless yields for K and L shells, *J. Phys. Chem. Ref. Data* **8**, 307 (1979).
- [56] F. von Busch, U. Kuetgens, J. Doppelfeld, and S. Fritzsche, $L_{23}[L_{23}] - MM[L_{23}]$ and $L_{23}[M^2] - MM[M^2]$ Auger vacancy satellite spectra of argon, *Phys. Rev. A* **59**, 2030 (1999).
- [57] R. D. Deslattes, E. G. Kessler, Jr., P. Indelicato, L. de Billy, E. Lindroth, J. Anton, J. S. Coursey, D. J. Schwab, C. Chang, R. Sukumar, K. Olsen, and R. A. Dragoset, X-ray transition energies ver. 1.2, <http://physics.nist.gov/XrayTrans>.
- [58] M. H. Chen, B. Crasemann, and H. Mark, Relativistic radiationless transition probabilities for atomic K- and L-shells, *At. Data Nucl. Data Tables* **24**, 13 (1979).
- [59] J. C. Levin, C. Biedermann, N. Keller, L. Liljeby, C.-S. O, R. T. Short, R. T. Short, I. A. Sellin, and D. W. Lindle, Argon-Photoion–Auger-Electron Coincidence Measurements Following K-Shell Excitation by Synchrotron Radiation, *Phys. Rev. Lett.* **65**, 988 (1990).
- [60] S. M. Huttula, P. Lablanquie, L. Andric, J. Palaudoux, M. Huttula, S. Sheinerman, E. Shigemasa, Y. Hikosaka, K. Ito, and F. Penent, Decay of a 2p Inner-Shell Hole in an Ar⁺ Ion, *Phys. Rev. Lett.* **110**, 113002 (2013).
- [61] A. G. Kochur, Final-ion-charge spectra produced by cascading decay of hollow argon and krypton atoms, *J. Electron. Spectros. Relat. Phenomena* **114**, 81 (2001).
- [62] M. Žitnik *et al.*, Two-to-one Auger decay of a double L vacancy in argon, *Phys Rev A* **93**, 021401(R) (2016).
- [63] F. von Busch, J. Doppelfeld, C. Gunther, and E. Hartmann, Argon L23-MM Auger satellite spectrum emitted after K ionization, *J. Phys. B* **27**, 2151 (1994).
- [64] P. Linusson, S. Fritzsche, J. H. D. Eland, M. Mucke, and R. Feifel, Single-photon multiple ionization forming double vacancies in the 2p subshell of argon, *Phys. Rev. A* **87**, 043409 (2013).
- [65] A. Kramida, Y. Ralchenko, J. Reader and NIST ASD Team (2022), NIST Atomic Spectra Database Ver. 5.8 (National Institute of Standards and Technology, Gaithersburg, MD, 2023), <https://physics.nist.gov/asd>.
- [66] E. B. Saloman, Energy levels and observed spectral lines of ionized argon, Ar II through Ar XVIII, *J. Phys. Chem. Ref. Data* **39**, 033101 (2010).
- [67] I. Velchev, W. Hogervorst, and W. Ubachs, Precision VUV spectroscopy of Ar I at 105 Nm, *J. Phys. B* **32**, L511 (1999).
- [68] J. E. Sansonetti and W. C. Martin, Handbook of basic atomic spectroscopic data, *J. Phys. Chem. Ref. Data* **34**, 1559 (2005).
- [69] V. Kaufman and W. Whaling, Improved wavelengths and energy levels of doubly-ionized argon (Ar III), *J. Res. Natl. Inst. Stand. Technol.* **101**, 691 (1996).
- [70] E. Biémont, Y. Frémat, and P. Quinet, Ionization potentials of atoms and ions from lithium to tin ($Z = 50$), *At. Data Nucl. Data Tables* **71**, 117 (1999).
- [71] S. Bashkin and J. O. Stoner, *Atomic Energy Levels and Grotrian Diagrams: Hydrogen I–Phosphorus XV* (Elsevier, Amsterdam, 2013).